Subsurface and Atmospheric Influences on Solar Activity
ASP Conference Series, Vol. 383, ©2008
R. Howe, R. W. Komm, K. S. Balasubramaniam, and G. J. D. Petrie, eds.

Role of Magneto-Convection in Plasma Dynamic and Energy Balance Above the Supergranular Network

T. Aiouaz

High Altitude Observatory, National Center for Atmospheric Research, PO Box 3000, Boulder CO 80307-3000, USA

Abstract. The current project aims to model the upper solar atmosphere taking in account the magnetic complexity of the supergranulation pattern. The result of a potential field extrapolation is used as the initial condition for the magnetic field in the framework of a forward 3D MHD model including the calculation of EUV emission lines. The MHD model describes the solar atmosphere from the high chromosphere to the lower solar corona above a synthetic supergranular cell. I present preliminary results on the relation between the magnetic topology, the thermodynamic properties of the plasma (e.g., flow, temperature, density) and the EUV intensity as calculated from the synthetic emission lines. Signatures of the magnetic field concentration is to be found in the corona in the density and temperature structure, and thus in emissivity and intensity, while the magnetic field is almost homogeneous. This model succeeds in reproducing for the first time the supergranular pattern as observed with a spectrometer in the EUV.

1. Introduction

The solar magnetic field has its footpoints in the photosphere, and extends through the chromosphere and transition region, to finally fill the whole corona. Early models of the solar atmosphere assumed simple plane-parallel geometry. Since it is clear from the observed structuring that the magnetic field plays a role, these simple models were modified to include the effect of the magnetic field (Gabriel 1976). The magnetic field in the quiet solar chromosphere is concentrated along the lanes of the supergranular network. From this chromospheric network magnetic funnels do emerge, and rapidly expand some 2–10 Mm above the photosphere to finally fill the whole corona. This causes the emission patterns of the chromospheric network to become wider with increasing temperature (e.g., Patsourakos et al. 1999). Later models (see Athay 1981, 1982) implicitly include the assumption that the magnetic field within the network is unipolar over supergranular scales. However Dowdy, Rabin, & Moore (1986) have argued that the observed fine scale structure of the network consists of mixed magnetic polarities. This led them to propose an alternative magnetic "junkyard" picture of the solar atmosphere, consisting of coronal funnels and network loops. Moreover, network field concentrations are surrounded by numerous weak mixed-polarity internetwork magnetic field on the scale of granulation. The convection-driven reprocessing of the magnetic field on the solar surface has led to the idea that small magnetic flux elements contribute significantly through reconnection to

the energy balance in the solar atmosphere (Parker 1991; Axford et al. 1999; Priest & Schrijver 1999; Priest, Heyvaerts, & Title 2002).

To study the properties of the solar atmosphere and the role of the magnetic field in the observed structuring of the supergranular network, a 3D magneto-hydrodynamic (MHD), time dependent, model is employed including the solar atmosphere all the way from the high chromosphere to the low corona. The energetics of the plasma include radiative losses, thermal conduction and a prescribed heating term. From the results of the MHD calculation we derive the resulting profiles of emission lines using the CHIANTI database (Dere et al. 1997; Young et al. 2003). The main goal of our investigation is to find out whether an observable (e.g., intensity, Doppler shifts) could be used as a diagnostic tool to investigate the heating mechanism in the corona.

2. The Model

Since Gabriel (1976) most models have incorporated a magnetic field as the primary cause of the atmosphere geometry. However, most of these models assume a magnetostatic configuration where the field passively channels thermal conduction and particles along the magnetic field lines. The most complete method to calculate the atmosphere geometry is to use the full set of MHD equations, which we will discuss in more detail in the following sections.

2.1. 3D Magnetic Junkyard

Supergranular cells are distributed fairly uniformly over the solar disk with a horizontal scale of approximately $20 - 30$ Mm. A horizontal plane is tiled periodically with hexagonal cells 20 Mm in diameter and surrounded by 2 Mm wide lanes to constitute a synthetic magnetogram. The network lanes (delineated with long dashed lines in the left panel in Figure 1) are the seed areas for a random distribution of strong network magnetic field concentrations. Concentrations of mixed polarity are randomly placed within the network (left panel in Fig. 1). A background field is added which consists of weak magnetic field concentrations of mixed polarity randomly distributed within the cells. Finally a potential field extrapolation of the synthetic photospheric magnetogram is carried out (see details in Aiouaz & Rast 2006). This magnetic field geometry allows us to study the effects of loops within the network area, of small loops with one foot point within the network and the other without, and of a mixture of funnels (see right panel in Fig. 1) on the solar atmosphere.

2.2. MHD Model

The evolution of the plasma is studied using the conservative form of the MHD equations:

$$\frac{\partial \rho}{\partial t} + \nabla\cdot(\rho \mathbf{v}) = 0 \tag{1}$$

$$\frac{\partial(\rho \mathbf{v})}{\partial t} + \nabla\cdot\left[\rho \mathbf{v}\mathbf{v} + \left(p_{\rm th} + \frac{B^2}{2\mu_0}\right)\mathbf{I} - \frac{\mathbf{B}\mathbf{B}}{\mu_0}\right] = \mathcal{F} \tag{2}$$

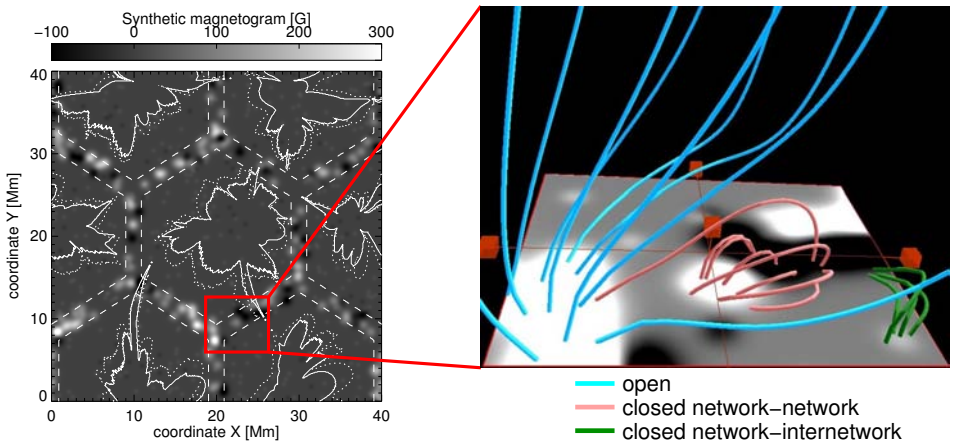

Figure 1. The network is composed of strong magnetic field concentrations. The internetwork field is a weak background field with a total background flux equal to zero. *Left:* The gray scale indicates the magnetic field strength. The *long dashed* lines delineate the seed area for the strong network magnetic field concentrations, assumed to be the network lanes. The *solid* and *dashed* lines are contours of the network mask calculated from the network expansion model (Aiouaz & Rast 2006) at height $z = 3\,\mathrm{Mm}$ and $z = 10\,\mathrm{Mm}$ respectively. *Right:* Sample of magnetic lines calculated from a potential field extrapolation (images from the VAPoR visualization software, Clyne & Rast 2005).

$$\frac{\partial \mathbf{B}}{\partial t} + \nabla\cdot(\mathbf{vB} - \mathbf{Bv}) = 0 \tag{3}$$

$$\frac{\partial e}{\partial t} + \nabla\cdot\left[\mathbf{v}\left(e + p_{\mathrm{th}} + \frac{B^2}{2\mu_0}\right) - \frac{(\mathbf{v}\cdot\mathbf{B})\mathbf{B}}{\mu_0}\right] = \mathbf{v}\cdot\mathcal{F} + \mathcal{S} \tag{4}$$

where the total energy density is given by $e = \frac{\rho v^2}{2} + \frac{p_{\mathrm{th}}}{\gamma - 1} + \frac{B^2}{2\mu_0}$. The variables are the density ρ, the momentum $\rho\mathbf{v}$, the total energy density e, and the magnetic field $\mathbf{B}$. In the right hand side of equation (2), $\mathcal{F}$ is a force which represents the effects of gravity and viscosity. It is defined as $\mathcal{F} = \rho\mathbf{g} - \nabla\cdot(\nu\Pi)$, where $\mathbf{g}$ is the gravitation field, ν the dynamic viscosity given for a fully-ionized H plasma by Spitzer (1962), and Π the dynamic pressure tensor. In the right hand side of equation (4), $\mathcal{S}$ is describing further sources and sinks:

$$\mathcal{S} = \nabla\cdot\mathbf{q} + L_{\mathrm{rad}} + H \quad [+C_{\mathrm{N}}]. \tag{5}$$

Here the heat conduction, $\nabla\cdot\mathbf{q}$, is along the magnetic field and follows the Spitzer law (Spitzer 1962). The radiative losses, L_{rad}, are assumed to have the tabulated form given by Rosner, Tucker, & Vaiana (1978) for an optically thin medium. To maintain a corona against conductive, radiative, and solar wind losses we specify a parametrized heating function H. This heating term varies with height z only (vertical direction) decreasing exponentially in the corona (see Serio et al. 1981). The last term of the energy sources and sinks in equation (5), in brackets, represents the Newton's law of cooling states, $C_{\mathrm{N}} = K(\rho/\rho_1^{(0)})^{\alpha}(T - T^{(0)})$, where $\rho_1^{(0)}$ is the density at $t = 0$ at the bottom boundary, $T^{(0)}$ is the temperature at

$t = 0$, K and α are adjustable constants which controls the area at the bottom boundary where $C_{\rm N}$ is not negligible ($K = 3$, $\alpha = 4$). This term prevents the chromosphere from completely disappearing from the computational domain in the case of too high heating. This ensures the numerical stability of the calculation by preserving chromospheric temperature at the bottom boundary. Newton cooling acts only on the few first cells of the computational domain due to the high value of α and to the exponential decrease of the density with z (height).

2.3. Initial and Boundary Conditions

As the initial condition for the magnetic field we use the potential field extrapolation as defined previously (see Fig. 1). The density, ρ, and the thermal pressure, $p_{\rm th}$, are initially defined using the hydrostatic pressure balance after the temperature is prescribed as an hyperbolic tangent. The velocity is set equal to zero everywhere in the domain.

The boundary conditions consist of an impenetrable bottom boundary, an open top boundary, and periodic side boundaries. At the lower boundary we keep the momentum and the horizontal gradient of the magnetic field equal to its value at $t = 0$. Additionally the total energy e and the vertical component of the magnetic field are set constant. Thus the chromosphere plays the role of a solid-wall for downward propagating waves, and the global magnetic structure of the atmosphere remains throughout the simulation. While there may be outgoing waves that should leave the domain properly without generating spurious reflections at the upper boundary, the top boundary is open. This means that the momentum and the gradient of the vertical component of the magnetic field are linearly extrapolated. The total energy at the top is set such that the gradient of the temperature at the top is zero to avoid heat flux into the domain. The horizontal boundaries are periodic.

2.4. Numerical Method

In the calculations presented here, the state of the plasma is predicted using the conserved form of the MHD equations. To solve this set of equations, we used the Versatile Advection Code (VAC) (Tóth 1996). Spatial and temporal discretizations are all second-order accurate. For our simulation we chose the TVD Lax-Friedrich scheme, which is more robust than the TVD scheme but also more diffusive. Since our simulation involved very steep gradients in the TR a high robustness was desired.

In multidimensional MHD the numerical conservation of $\nabla\cdot\mathbf{B}$ is not guaranteed by TVD type schemes. Therefore $\nabla\cdot\mathbf{B}$ is kept close to zero every few time steps using the projection scheme. This way, the error cannot grow and the number of iterations to achieve this accuracy is relatively small. Additionally, the Powell's scheme is used to advect out the effect of the remaining non-divergence free magnetic field.

3. The Spectral Code

At this point we assume ionization equilibrium to calculate the line emission. As our velocities are quite moderate compared to ionization times this is a possible

simplification (see Peter, Gudiksen, & Nordlund 2004). Under this assumption the emissivity of an optically thin spectral line is defined as

$$\varepsilon_{\rm ji} = h\nu_{\rm ji}\, A_{\rm ji}\, n_{\rm j} \quad [{\rm W}\cdot{\rm m}^{-3}],$$

where i, j are the lower and upper levels, $A_{\rm ji}$ is the spontaneous transition probability, $n_{\rm j}$ is the number density of the upper level j of the emitting ion.

The spectral code uses as input the values of density ρ, temperature T, and the plasma flow $v_{\rm z}$ along the line of sight z, values provided by the 3D MHD solutions. The ion emissivity, $\varepsilon_{\rm ji}$, is computed at each grid point of the computational domain using the CHIANTI database (Dere et al. 1997; Young et al. 2003). Once the ion emissivities are calculated, a normalized Gaussian profile is associated at each grid point to calculate emission profiles ε_ν, defined as

$$\varepsilon_\nu = \frac{\varepsilon_{\rm ji}}{\pi^{1/2}\Delta v_{\rm D}} \exp\left[-\frac{v_{\rm z}^2}{\Delta v_{\rm D}^2}\right].$$

Here the Doppler width $\Delta v_{\rm D} = (2kT/M_{\rm i})^{1/2}$ is calculated using the temperature, and the Doppler shift using the velocity along the line of sight $v_{\rm z}$. $M_{\rm i}$ is the mass of the considered ion. The emission line profiles are then integrated along the vertical direction (line-of-sight). From these integrated spectra along the line of sight (i.e., vertically) intensity, line width and line shift are extracted.

4. Results and Discussion

4.1. Relaxation to Quasi-Steady State

Magnetized plasmas relax when they seek their natural state of lowest energy subject to certain topological constraints imposed, e.g., by the magnetic field. Relaxation may be fast and dynamic or slow and gradual depending on the external environment in which the system evolves.

In our case, the plasma is set in the initial conditions in hydrostatic equilibrium, and the magnetic field in a potential equilibrium. However it is important to note that the coupled magnetohydrodynamic system is *not* in a state of lowest energy. The different energy terms are not balanced everywhere in the computational domain, thus the system evolves to a state of lower energy.

Since the model is dynamic the magnetic field evolves until a balance is reached between the magnetic pressure and the thermal pressure. In term of energy, the coupled magnetohydrodynamic system evolves until a balance is reached between the gains and the losses which appear in the energy equation. Figure 2 shows the temperature, the plasma flow and the magnetic field at $t \sim 10$ minutes (solar time). This preliminary state is strictly speaking a state of the asymptotic behavior tending to the quasi steady state. Such a convergence in VAC is followed by the evolution of the residual.

4.2. Thermodynamic Results

Beginning with hydrostatic pressure balance and a potential field, an advanced state is presented at $t \sim 10$ minutes of solar time, which represents approximately two sound travel times. The panels in Figure 2 show in gray scale

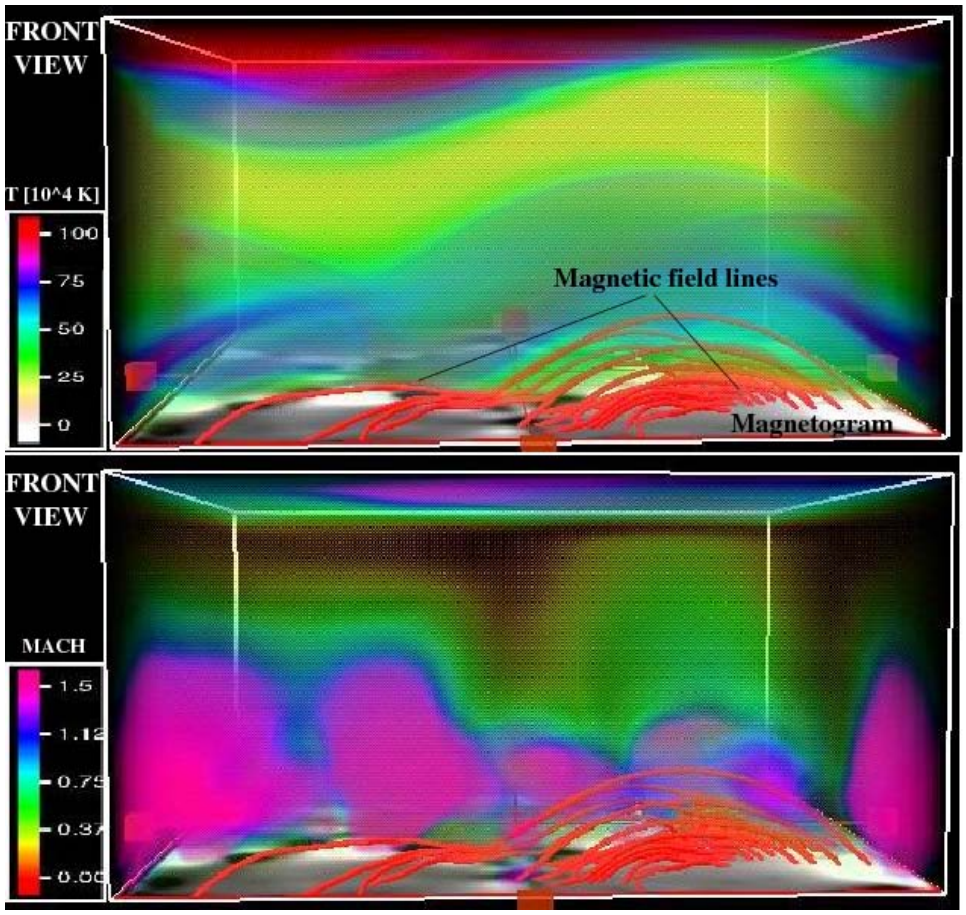

Figure 2. Snapshot images of a preliminary MHD simulation computed with the VAC code at $t \sim 10$min (solar time). The red lines show a sample of magnetic lines. The gray scale of the bottom layer indicates the magnetic field strength of the synthetic magnetogram (see Fig. 1 for a top view). The color scale indicates the plasma temperature (upper panel). The color scale indicates the mach number (lower panel) (images from the VAPoR visualization software, Clyne & Rast 2005).

a snapshot of the temperature (upper) and a snapshot of the mach number (lower). The solid lines represent a sample of magnetic field lines.

A first look at the results shows that the temperature is highly structured in the computational domain even though it remains globally stratified. A closer look at the results shows loop-like structures following the magnetic field lines. These properties are expected from observations and mainly due to the thermal conduction, which is by far the most efficient heat transfer mechanism at these temperatures. The heat from the corona is conducted deep into the "cold" atmosphere following the open magnetic field lines. This shows the crucial role played by the magnetic field topology. The conduction moves the transition region toward higher densities until it reaches a balance with radiative cooling, which is proportional to the square of the density. In the closed magnetic field

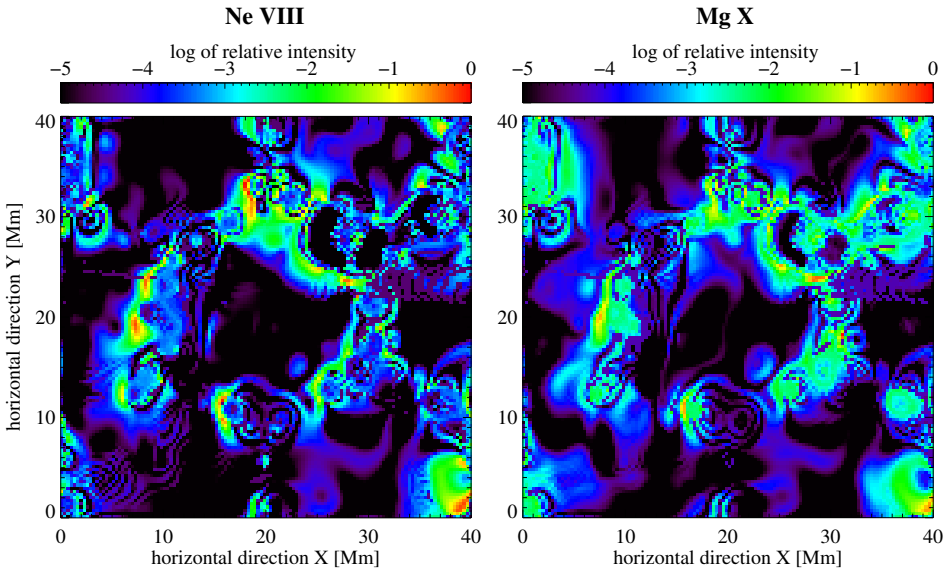

Figure 3. Intensities corresponding to Figure 2 computed with the spectral code for optically thin emissions lines in the high transition region (*left*, Ne VIII) and in the corona (*right*, Mg X).

areas, when the loops do not reach coronal temperature, the topology does not allow any thermal connection between the chromosphere and the corona, and thus does not allow any heat transfer between the closed magnetic field areas and the corona, thus maintaining the transition region higher up in the atmosphere.

Moreover, plasma flows (lower panel) seem stronger toward open magnetic field areas. Hammer (1982) established that the variation of the thermal pressure, cause of the velocity variation along the magnetic field lines, is related to the heating (see details in Aiouaz, Peter, & Keppens 2005). This property is commonly observed in the solar corona when looking at coronal lines above quiet-Sun areas. The internetwork region shows on average less outflow than the network where the magnetic field is concentrated (Aiouaz, Peter, & Lemaire 2005). However, to be able to compare this result with observations in the upper transition region or low corona, we must now look at results of the synthetic spectra calculated from these thermodynamical results.

4.3. Spectral Results

The panels in Figure 3 present the intensities for the Ne VIII (left) and Mg X (right) emission line, as it would be observed from a spectrometer. It clearly shows for the first time that the magnetic field concentrated in the chromosphere strongly influences observables in the corona. This result supports recent observational results on chromospheric footprints of the solar wind (McIntosh & Gurman 2005). Furthermore it reproduces astonishingly well the supergranular network as observed with EUV spectrometers. The strongest intensity originates from the network lanes, even though the strongest intensities do not seem to come from the strongest magnetic field strength areas. Blinking the left

(Ne VIII) and right (Mg X) panel clearly shows the expansion of the network with increasing temperature of formation. At this point we can only speculate on the exact reason for these intensity variations. Nevertheless these results are encouraging as it is the first time a model recreates the network pattern as observed in the EUV.

5. Outlook

The model presented above is the first forward 3D MHD model of the upper solar atmosphere which succeeds in recreating a supergranular pattern as observed with a spectrometer in the EUV. This result is of major importance because it gives a diagnostic tool for the investigation of the heating mechanism in the corona. It directly relates the heating form to the thermodynamical *and* spectral properties of the plasma. Results from the simulations will be compared directly to spectroscopic (e.g., SUMER/SOHO, EIS/Hinode) and polarimetric (e.g., DST, SOLIS) observations. Most importantly these simulations will augment significantly interpretations of the high resolution and high sensitivity observations from recently launched (e.g., STEREO, Hinode) missions.

References

Aiouaz, T., Peter, H., & Keppens, R. 2005, A&A, 442, L35
Aiouaz, T., Peter, H., & Lemaire, P. 2005, A&A, 435, 713
Aiouaz, T. & Rast, M. 2006, ApJ, 647, L183
Athay, R. G. 1981, ApJ, 249, 340
Athay, R. G. 1982, ApJ, 263, 982
Axford, W. I., McKenzie, J. F., Sukhorukova, G. V., Banaszkiewicz, M., Czechowski, A., & Ratkiewicz, R. 1999, Space Sci.Rev., 87, 25
Clyne, J. & Rast, M. 2005, in Visualization and Data Analysis 2005, ed. R. F. Erbacher, J. C. Roberts, M. T. Grohn, & K. Borner, Proc. SPIE, 284, `http://www.vapor.ucar.edu`
Dere, K. P., Landi, E., Mason, H. E., Monsignori Fossi, B. C., & Young, P. R. 1997, A&AS, 125, 149
Dowdy, J. F., Rabin, D., & Moore, R. L. 1986, Solar Phys., 105, 35
Gabriel, A. H. 1976, Phil. Trans. R. Soc. Lond. A., 281, 339
Hammer, R. 1982, ApJ, 259, 779
McIntosh, S. W., & Gurman, J. B. 2005, Solar Phys., 228, 285
Parker, E. N. 1991, ApJ, 372, 719
Patsourakos, S., Vial, J.-C., Gabriel, A. H., & Bellamine, N. 1999, ApJ, 522, 540
Peter, H., Gudiksen, B. V., & Nordlund, Å. 2004, ApJ, 617, L85
Priest, E. R., Heyvaerts, J. F., & Title, A. M. 2002, ApJ, 576, 533
Priest, E. R. & Schrijver, C. J. 1999, Solar Phys., 190, 1
Rosner, R., Tucker, W. H., & Vaiana, G. S. 1978, ApJ, 220, 643
Serio, S., Peres, G., Vaiana, G. S., Golub, L., & Rosner, R. 1981, ApJ, 243, 288
Spitzer, L. 1962, Physics of Fully Ionized Gases, New York: Interscience (2nd edition)
Tóth, G. 1996, Astrophys. Lett., 34, 245
Young, P. R., Del Zanna, G., Landi, E., et al. 2003, ApJ, 144, 135